Water Science & Technology

IWA PUBLISHING

Water Science & Technology Vol 84 No 7, 1757 doi: 10.2166/wst.2021.358

Selective adsorption of phosphate by carboxyl-modified activated carbon electrodes for capacitive deionization

Luwei Miao [a], Wenyang Deng [b], Xiaohong Chen [a], Ming Gao [a], Wenqing Chen [a,*] and Tianqi Ao [c,d]

[a] College of Architecture and Environment, Sichuan University, Chengdu 610065, China
[b] Institute for Disaster Management and Reconstruction, Sichuan University-The Hong Kong Polytechnic University, No. 122, Section 1 Yellow River Middle Road, Chengdu 610065, Sichuan, China
[c] State Key Laboratory of Hydraulics and Mountain River Engineering, Sichuan University, Chengdu, 610065, China
[d] College of Water Resource and Hydropower, Sichuan University, Chengdu, 610065, China
*Correspondence author. E-mail: scu_cwq@163.com

LM, 0000-0002-9589-0100; WD, 0000-0002-9589-0100; XC, 0000-0002-9589-0100; MG, 0000-0002-9589-0100; WC, 0000-0002-9589-0100; TA, 0000-0002-9589-0100

ABSTRACT

Capacitive deionization (CDI) has been considered as a promising technology for removing phosphate from water but suffer inferior selectivity and electrosorption performances for phosphate of current carbon electrodes in CDI. Herein, we achieved highly selective phosphate removal from a ternary effluent of Cl^-, PO_4^{3-}, and SO_4^{2-} by using nitric acid-treated activated carbon (AC) with various modification times and pure AC as the anode and cathode, a novel phosphate selective asymmetric CDI reactor. The results showed that carboxyl groups greatly grafted on the materials after modification (varying from 0.00084 to 0.0012 mol g^{-1}). The phosphate selectivity of the present research was higher than that of unmodified CDI, and it increased with the increase of carboxyl groups content. The highest phosphate selectivity (2.01) in modified materials is almost six times higher than that of pure AC. Moreover, the modified electrodes exhibited good regenerative ability with a phosphate desorption efficiency of around 72.12% during the adsorption/desorption process and great stability during the cycling experiment. These results demonstrated that the innovative application of nitric acid-modified AC can effectively selectively remove phosphate from mixed anion solution, opening a hopeful window to selective adsorption in water treatment by CDI.

Key words: activated carbon electrode, capacitive deionization, carboxyl groups, desalination, selective adsorption

HIGHLIGHTS

- Using nitric acid-modified AC for phosphate adsorption when applying to CDI anode.
- Nitric acid treatment could improve the adsorption capacity of phosphate.
- The effect of hydrogen-bond interaction on selectively adsorption was discussed.
- AC-3 exhibits great cyclability and excellent stability.

GRAPHICAL ABSTRACT

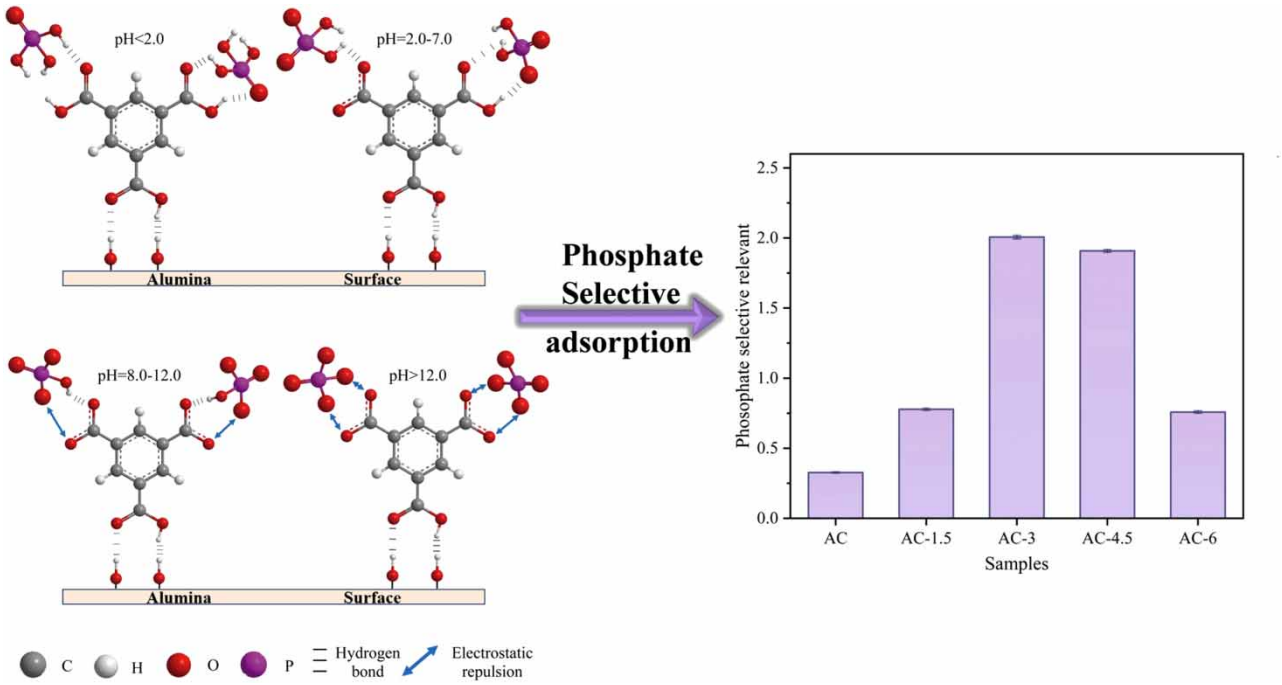

1. INTRODUCTION

Excessive phosphorus originated from industrial wastewater, domestic sewage and farmland drainage released into water may speed up water eutrophication and aquatic species biodiversity decrease, threaten human health and increase water treatment cost (Jiang *et al.* 2019; Zheng *et al.* 2021). Water blooms have frequently emerged in China and Southeast Asia recently due to phosphorus concentrations exceeding the World Health Organization (WHO) recommended standard of 5 mg L^{-1} (Sakamoto *et al.* 2020). Hence, removing excess phosphorus from water has become an essential and urgent issue (Liu *et al.* 2018). Many technologies are currently available for treating phosphorus-rich water, including physical methods, chemical methods and bioanalysis (Song *et al.* 2019). However, these methods might suffer from some defects. Chemical precipitation processes may be costly and cause secondary pollution when treating phosphorus wastewater (Lei *et al.* 2021) and physical adsorption methods often have low selectivity for phosphate (Paltrinieri *et al.* 2019). A new and promising deionization technique, capacitive deionization (CDI), can improve these drawbacks based on its multiple advantages of cost-effective, eco-friendly, energy-efficient and easy generation. Especially, it has potential to satisfy the demand for improving selective adsorption of phosphate via strategically designing proper electrode materials (Mohamed *et al.* 2020; Tian *et al.* 2021).

CDI is a novel and benign electrosorption technology that functions by applying a voltage between a pair of electrodes and was developed recently for water treatment (Li *et al.* 2014). The mechanism of CDI is that ions are electrosorbed by charged porous carbon electrodes via electrochemical double-layer capacitors (EDLCs), which form when an external voltage is supplied. After deionization, the captured ions are released easily by reversing or short-circuiting the applied voltage (Wu *et al.* 2021). Apart from being mainly applied in desalination, CDI has been proven to be available for removing heavy metals (Kyaw *et al.* 2020) and anions in wastewater (Wang *et al.* 2018), for water softening (Liu *et al.* 2020), and for water sterilization (Xing *et al.* 2020). Most recently, CDI has been studied by many researchers because of its high feasibility and potential in the field of removing phosphate. A study succeeded in carrying out the goal of attaining phosphate adsorption by taking advantage of magnetic carbon electrodes with 10 wt% Fe_3O_4 in CDI (Zhang *et al.* 2021). Jiang successfully demonstrated phosphate removal in the CDI process with a layered double hydroxide/reduced graphene oxide (LDH/rGO) composite electrode in water (Hong *et al.* 2020). However, these reported works did not closely reflect the real ionic composition present in domestic wastewater, considering the complexity of the coexistence of other ions. Simultaneously, few researchers have systematically

investigated how to improve adsorption selectivity toward phosphate, as it is not always necessary to remove all the anions in wastewater (Kim & Choi 2012). Hence, the greatest challenge and the best goal for CDI is to obtain an electrode material that could effectively and selectively adsorb specific ions from a solution containing several anions. The use of specific ion-selective carbon electrodes could make operation easier, decrease costs, and widen its applications, since only the specific target ions are removed (Sun *et al.* 2021).

Numerous studies have now reported that many materials, such as activated carbon (AC) (Wang *et al.* 2018), carbon nanofibers (He *et al.* 2020), and carbon nanotubes (Zhao *et al.* 2020), can be used in CDI. Among these materials, AC has become the most competitive electrode material for large-scale CDI applications due to its huge specific surface area, well developed pore structure, surface chemical functional groups and excellent electrical conductivity (Chen *et al.* 2015; Yasin *et al.* 2017). To improve its adsorption performance and widen its application extent, numerous modification methods, including physical and chemical methods, have been gradually developed (Yasin *et al.* 2017; Sufiani *et al.* 2020). Chemical surface modification methods are extensively used to prepare electrodes with better performance, which can be realized by using nitric acid (Yao *et al.* 2016), hydrogen peroxide (Roh *et al.* 2018), and sulphuric acid (Zhao *et al.* 2019) treatments. They could improve the adsorption capacity of AC by modifying its surface functional groups. Acidic treatment can change the category of oxygen surface functional groups by using oxidizing agents and introducing new acidic groups on AC (Huang *et al.* 2009). Nitric acid modification is a valuable surface modification technology for AC because it can more successfully introduce carboxyl groups than others, with additional features of a simple process and lower costs (Huang *et al.* 2009; Yu *et al.* 2013; Huang *et al.* 2014). Yao *et al.* reported that rice husk-based AC treated with nitric acid exhibited good Pb(II) adsorption performance (Yao *et al.* 2016). Currently, although the modified materials have exhibited good ion adsorption properties, there are few reports about applying nitric acid-treated AC to anodes for adsorbing anions in CDI because carboxyl groups are negatively charged. The corresponding studies in regard to selective removal are also limited. Herein, in order to overcome this limitation, the use of carboxyl-modified activated carbon as a CDI cathode to selectively adsorb phosphate is explored.

In this paper, nitric acid-fabricated AC and pure AC were studied as the cathode and anode electrodes in CDI for the selective removal of phosphate from solution, which has yet to be reported. The influence of AC modification time on CDI performance under identical positive electrodes was examined. This study thoroughly reports the fabrication, characterization, and electrochemical properties evaluation of the selective electrode, and further investigates its phosphate adsorption behavior and evaluates the reversible regeneration stability. With comprehensive analyses, this work demonstrates the feasibility of nitric acid-modified AC as a suitable sorption medium for the selective adsorption of phosphate from solution, providing a promising and valid theoretical guidance for target ion adsorption from solutions in future practical water treatment applications.

2. MATERIALS AND METHODS

2.1. Reagents and materials

Pure AC was bought from Chengde, Lijing Activated Carbon Manufacturing Company, China. All chemicals and solutions were of analytical grade and purchased from Kelon Chemical Reagent Factory (Chengdu, China), and they were used in the experiments without any further treatment. Nitric acid for AC treatment, sodium chloride for electrolytic solution preparation, *N,N*-dimethylacetamide (DMAC) and polyvinylidene fluoride (PVDF) as the binder for electrode preparation used in the work were from Arkema Chemical Company (France). Other main chemicals included sodium bicarbonate ($NaHCO_3$) for carboxyl content titration and sodium sulphate (Na_2SO_4) and sodium dihydrogen phosphate (NaH_2PO_4) for electrosorption/desorption experiments (Kelong Chemical Reagent Factory, Chengdu, China).

2.2. Modification of AC by nitric acid

The AC used in this work was modified by surface oxidation with nitric acid (HNO_3) (analytical grade, 32.5%, Kelon). The modification step was as follows (Figure 1(a)). Ten grams of AC was added to 300 mL of a 32.5% (v/v) HNO_3 solution. The mixture of the AC and acid solution was stirred well and heated to 90 °C for 1.5, 3, 4.5, and 6 h in a simple reflux system to reach different carboxyl group contents and degrees of oxidation for each material. The prepared AC-x (x = 1.5, 3, 4.5, 6) solid phase was separated by filtration, washed with distilled water until reaching a neutral pH and dried in an oven at 80 °C for 4 h. The modified samples were referred to as AC-1.5, AC-3, AC-4.5 and AC-6, respectively. For pure AC, after particle sieving, the untreated AC was washed with distilled water and dried in an oven at 80 °C for 4 h (named AC).

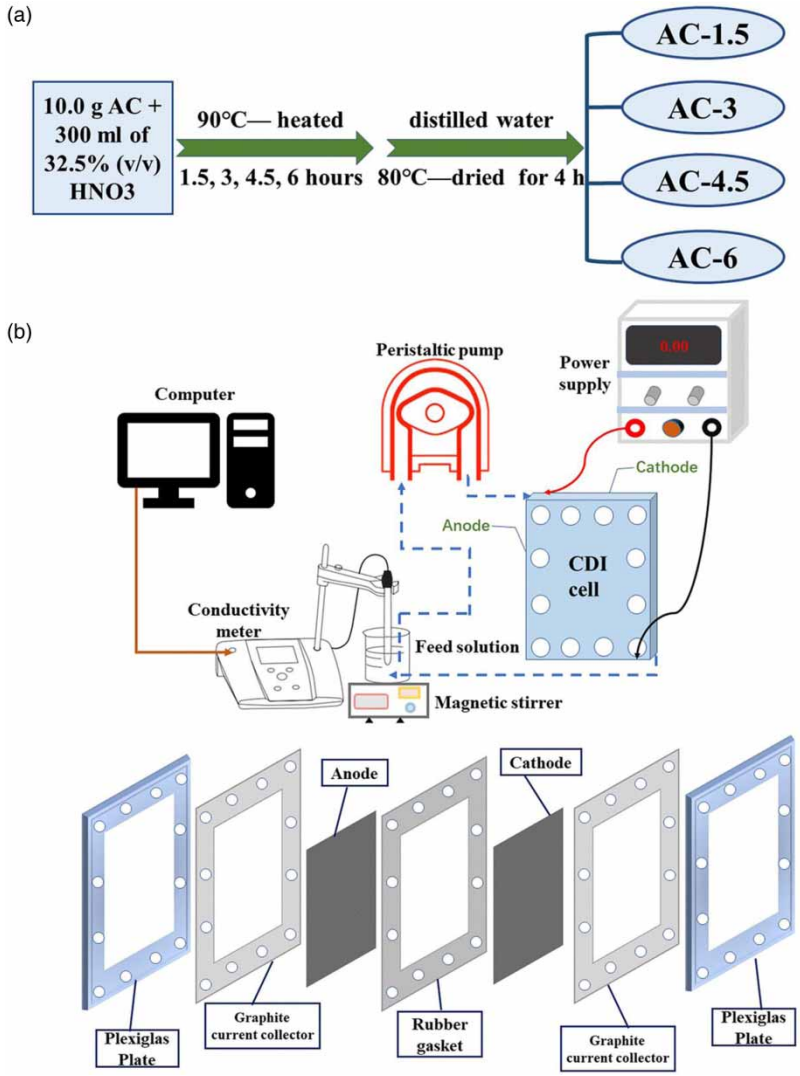

Figure 1 | (a) Schematic fabrication of nitric acid-treated electrodes; (b) schematic representation of the CDI system (upper) and of the CDI cell (lower).

2.3. CDI experimental set up

The CDI setup consisted of a CDI cell, a peristaltic pump, a conductivity meter and an external power supply. A schematic diagram of CDI setup is exhibited in Figure 1(b).

Specifically, in the process of preparing the electrodes, glutinous AC was prepared by mixing sieved AC powder, acetylene black and PVDF in a DMAC solution and stirring with a magnetic stirring apparatus for 10 h. Then, the slurry was uniformly cast on to a graphite plate to form electrodes with a size of 45*50*1 mm. The cast electrodes were dried at 60 °C for 8 h, and then in a vacuum oven for 2 h. The CDI cell was composed of a pair of square Plexiglas plates, a rubber gasket, a pair of graphite current collectors, and a pair of carbon electrodes, using the nitric acid-modified electrode and pure AC as the anode and cathode, respectively.

2.4. Desalination test

CDI experiments were all performed in the same mode for at least 1 h (Figure 1(b)). All of the electrodes had the following dimensions, 100 mm*100 mm*0.12 mm. The concentration, volume and flow rate of the sodium chloride (NaCl) solution were set as 200 mg L^{-1}, 100 and 30 mL min^{-1}, respectively. The applied voltage was 1.2 V. A specific description of the desalination procedure is given in Text S1.

2.5. Characterization

For overall tests, the morphologies of AC and AC-x were analyzed by scanning electron microscopy (SEM, JEOL JSM-7500F) combined with energy dispersive X-ray spectrometry (EDS, Aztec X-Max80) for postmortem analysis. The specific surface area and pore structure of the materials were characterized by nitrogen adsorption–desorption isotherms using a Kubo nitrogen adsorption apparatus (Biaode Elec. and Tech. Co., China). The specific surface area and the pore size distribution were derived by the Brunauer-Emmett-Teller (BET) method and the Barrett–Joyner–Halenda (BJH) method, respectively. The surface chemical characteristics were viewed by Fourier transform infrared (FTIR) spectroscopy (IRAffinity-1S) within a spectrum range of 4,000 to 500 cm^{-1}. The samples were analyzed by X-ray photoelectron spectroscopy (XPS) to determine and present their chemical structures and functional groups with an AXIS Supra XPS analyzer (UK). The zeta potential of materials was determined by a Zetasizer Nano ZS to analyze the surface electrical potential. For hydrophilia analysis, the surface wettability of AC and AC-x films was measured in terms of the static contact angle values using a goniometer (JC2000D2H Digidrop).

2.6. Electrochemical analysis

To estimate the electrochemical properties of the electrode materials, electrochemical experiments such as cyclic voltammetry (CV) and galvanostatic charge-discharge (GCD) within the defined potential window of −0.4 V to 0.8 V were performed on a CHI660E electrochemical workstation with a three-electrode cell using a 1 M NaCl solution. The temperature of the NaCl aqueous solution was kept at 298 K. Details of the electrochemical experiment are shown in Text S2.

2.7. Selective adsorption of phosphate and subsequent desorption experiments

In this step, Cl^-, PO_4^{3-}, and SO_4^{2-} solutions were prepared from NaCl, Na_2SO_4 and NaH_2PO_4, respectively. Throughout the study, the system was operated for 120 min for both the adsorption and desorption tests. During selectivity tests, to investigate of phosphate sorption selectivity under the coexistence of three anions, three mixed NaCl, NaH_2PO_4 and Na_2SO_4 solutions were used as feed solutions. The initial concentrations of NaCl, NaH_2PO_4 and Na_2SO_4 in the ternary solutions were all fixed at 0.8 mM. Samples were collected every 10 min and the concentrations of various anion components were then evaluated using Lc-20AD IC plus-ion chromatography. Experiments were carried out at room temperature with an external voltage of 1.2 V and a flow rate of 30 mL min^{-1}. Subsequently, a 60-min short circuit was used to effectively desorb anions, and the anions were analyzed by ion chromatography (IC, LC-20AD, Japan).

2.8. Analysis methods

To represent the electrochemical properties of each electrode, CV experiments were performed to determine the specific capacitance of the electrodes in accordance with Equation (1):

$$C = \frac{\int IdV}{2vm} \tag{1}$$

where C is the specific capacitance (F g^{-1}), I is the response current (A), m is the mass of the working electrode material (g), v is the potential scan rate (mV s^{-1}), and dV/v represents the potential window (V).

The CDI performance, including the salt adsorption capacity (SAC), was calculated in Equation (2):

$$SAC = \frac{V(C_0 - C)}{m} \tag{2}$$

where V is the solution volume (L), C_0 is the initial concentration (mg L^{-1}), C is the equilibrated concentration (mg L^{-1}), and m is the mass of the active electrode material (g).

To quantitatively analyze the anion removal performance, the adsorption capacity and removal ratio of the three anions were described by Equations (3) and (4), respectively:

$$SAC_{(Cl^-,PO_4^{3-},SO_4^{2-})} = \frac{(C_0 - C_e)V}{m} \tag{3}$$

$$Removal(\%) = \frac{C_0 - C_e}{C_0} \times 100\% \tag{4}$$

where SAC (Cl^-, PO_4^{3-}, and SO_4^{2-}) is the adsorption capacity of the anions (mmol g^{-1}), C_0 is the initial anion concentration (mg L^{-1}), C_e is the final anion concentration (mg L^{-1}), V represents the solution volume (L), and m is the mass of the electrode (g).

To evaluate the selective adsorption properties of the electrodes, the selectivity coefficient of PO_4^{3-} is determined in Equation (5):

$$K_{PO_4^{3-}} = \frac{C_{PO_4^{3-}}(C'_{Cl^-} + C'_{SO_4^{2-}})}{C'_{PO_4^{3-}}(C_{Cl^-} + C_{SO_4^{2-}})} \quad (5)$$

where C'_{Cl^-}, $C'_{PO_4^{3-}}$, $C'_{SO_4^{2-}}$ represent the concentration of each anion in the solution (mg L^{-1}), and C_{Cl^-}, $C_{PO_4^{3-}}$, $C_{SO_4^{2-}}$ represent the concentration of each anion adsorbed on the CDI cell (mg L^{-1}).

The desorption efficiency in the desorption process was calculated using Equation (6):

$$\text{Desorption effecience} = \frac{V(C_d - C_0)}{N} \quad (6)$$

where C_d is the concentration of anions at the end of desorption (mg L^{-1}), C_0 is the starting concentration of anions at the beginning of desorption (mg L^{-1}), V is the total volume of the desorbed solution (L), and N is the amount of anions adsorbed on the anode (mg).

3. RESULTS AND DISCUSSION

3.1. Characterization of electrodes

The surface structure is a vital physical factor that influences the sorption capacity of materials. Figure 2(a) and 2(b) and Figure S1 (shown in the Supporting Information) show the SEM images of AC-1.5, AC-3, AC-4.5 and AC-6 in comparison with that of pure AC, respectively. The surface of AC is rough and irregular with a dense, rough and uneven pore structure. However, the pores of AC are well developed, providing an abundance of available adsorption sites. As expected, the total amount of acidic groups on the surface increased after modification compared to pure AC. When the modification time ranges from 1.5 to 4.5 h, an enlarged pore size is clearly noted, and the mesoporous volume tends to increase considerably. Moreover, the particles on the surface become smaller and smoother after the modification process, indicating that the number of surface carboxyl groups on AC increases significantly. Regarding AC-6, the collapse of the pore structure demonstrated in this study is probably associated with the formation of a large number of oxygen-containing functional groups during the modification procedure (Huang *et al.* 2009; Verlicchi & Zambello 2015). It has been proven that oxygen-containing functional groups can plug the micropore inlet by being adsorbed on the inner surface of the pore, resulting in narrow pores and a decrease in the specific surface area and total pore volume (Chen *et al.* 2003; Shi *et al.* 2015).

The pore structure of the electrodes was determined via their nitrogen adsorption/desorption isotherms at 77 K (Figure 2(c)). According to the International Union of Pure and Applied Chemistry classification, the isotherms of AC and AC-x exhibit type IV adsorption performance (Liu *et al.* 2019). When the relative pressure is below 0.1, the nitrogen adsorption capacity increases sharply. A hysteresis loop appears with an upward trend when the relative pressure is between 0.7 and 1, indicating that all samples have a combination of microporous and mesoporous structures (Xiao *et al.* 2013; Liu *et al.* 2021a).

The pore size distributions of the five samples are depicted in Figure 2(d). The specific surface area, total pore volume, average pore diameter, mesopore volume and ratio of $V_{mesopore}$ to V_{total} are listed in Table 1. As illustrated, the surface area substantially increases from 629 to 681 m^2 g^{-1} as the modification time increases from 1.5 to 4.5 h, which confirms that carboxyl groups were successfully deposited on the AC surface. The total pore volume of AC and AC-x also rises by approximately 10% as the modification time increases from 1.5 to 4.5 h, possibly because HNO_3 utilization can enlarge the pores by etching the carbon atoms on the micropore wall (Xiao *et al.* 2013). This means that HNO_3 modification can provide more active sites for electrosorption and thus improve the electrochemical properties of electrode materials (Yu *et al.* 2013; Huang *et al.* 2014). Clearly, AC-3 has the largest specific surface area and largest pore volume, which is conducive to accelerating the ion transport rate and adsorption in CDI. In contrast, the surface area and the total volume of AC-6 decreased slightly compared with those of AC. This can be ascribed to the collapse of the channel (ShamsiJazeyi & Kaghazchi

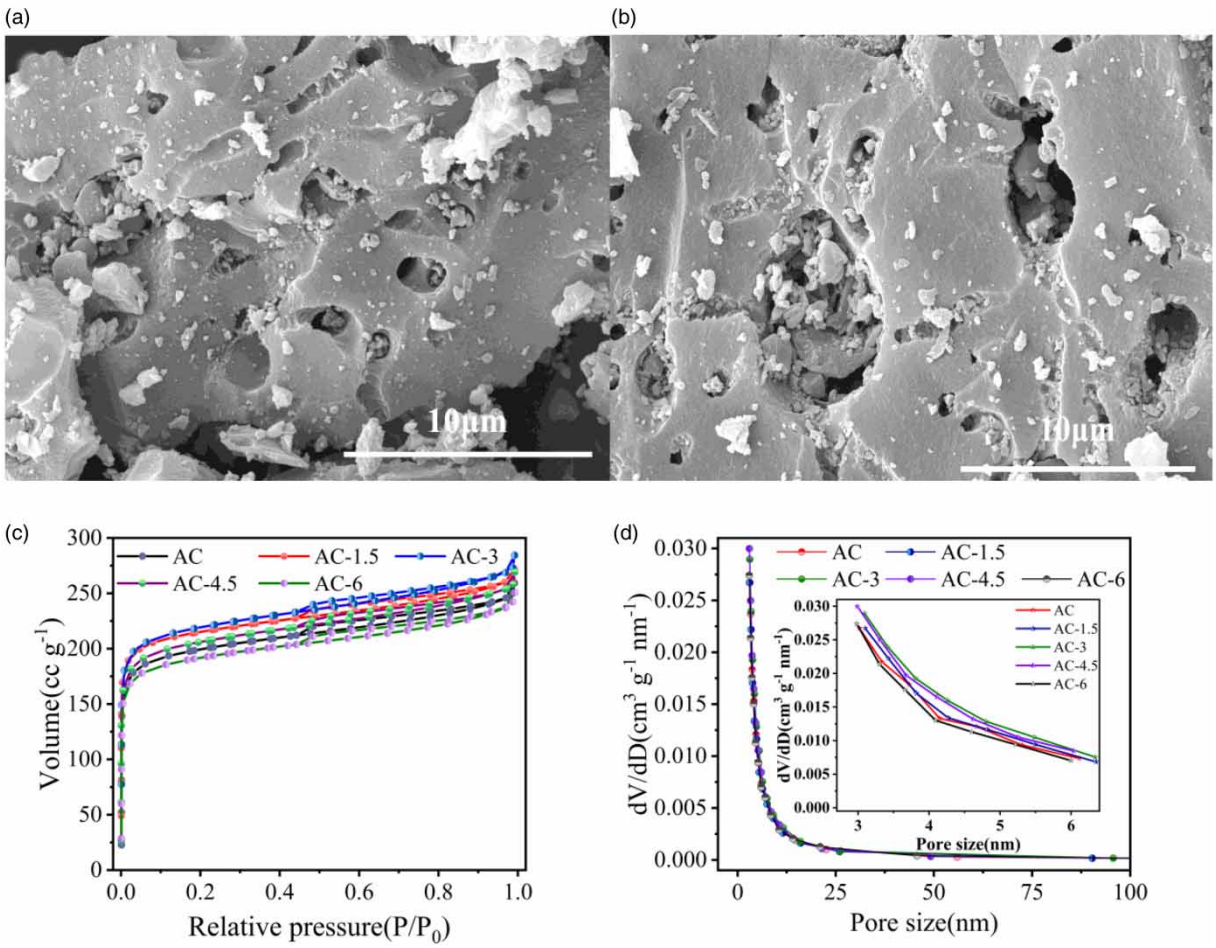

Figure 2 | SEM images of (a) AC and (b) AC-3; (c) nitrogen adsorption–desorption isotherms of five samples, and (d) the pore size distributions of the five materials. The inset shows the pore size distributions of all samples in the range of 2–7 nm.

Table 1 | Pore structure parameters of five materials

Material	Specific surface area($m^2 \cdot g^{-1}$)	Total pore volume ($cm^3\ g^{-1}$)	Average pore diameter (nm)	Mesopore volume ($cm^3\ g^{-1}$)	Ratio of $V_{mesopore}$ to V_{total}
AC	629	0.4099	2.60	0.0901	22.19%
AC-1.5	632	0.3913	2.48	0.0886	22.64%
AC-3	681	0.4305	2.52	0.1001	23.25%
AC-4.5	679	0.4281	2.52	0.1059	24.74%
AC-6	617	0.3902	2.52	0.0979	25.09%

2010), which is consistent with the SEM characterization result. Furthermore, the average pore sizes of the materials at different modification times are between 2.48 and 2.52 nm, and the ratio of $V_{mesopore}$ to V_{total} increases by around 2.9%. The raising proportion of mesoporous volume in terms of the total volume can enhance the ion transport rate, leading to a higher salt capacity (Yeh *et al.* 2015).

The FTIR spectra of the fabricated electrodes are listed in Figure 3(a). The bands at 1,528 cm^{-1} and 1,719 cm^{-1} are related to the antisymmetric stretching vibrations of carboxyl groups and the specific peak for the stretching vibrations of C = O bonds in carboxylic acid functional groups, respectively (Yu *et al.* 2013; Gokce & Aktas 2014). Based on the FTIR data, a weak stretching vibration of OH was observed at 2,300 cm^{-1}, as reported in the literature (ShamsiJazeyi & Kaghazchi

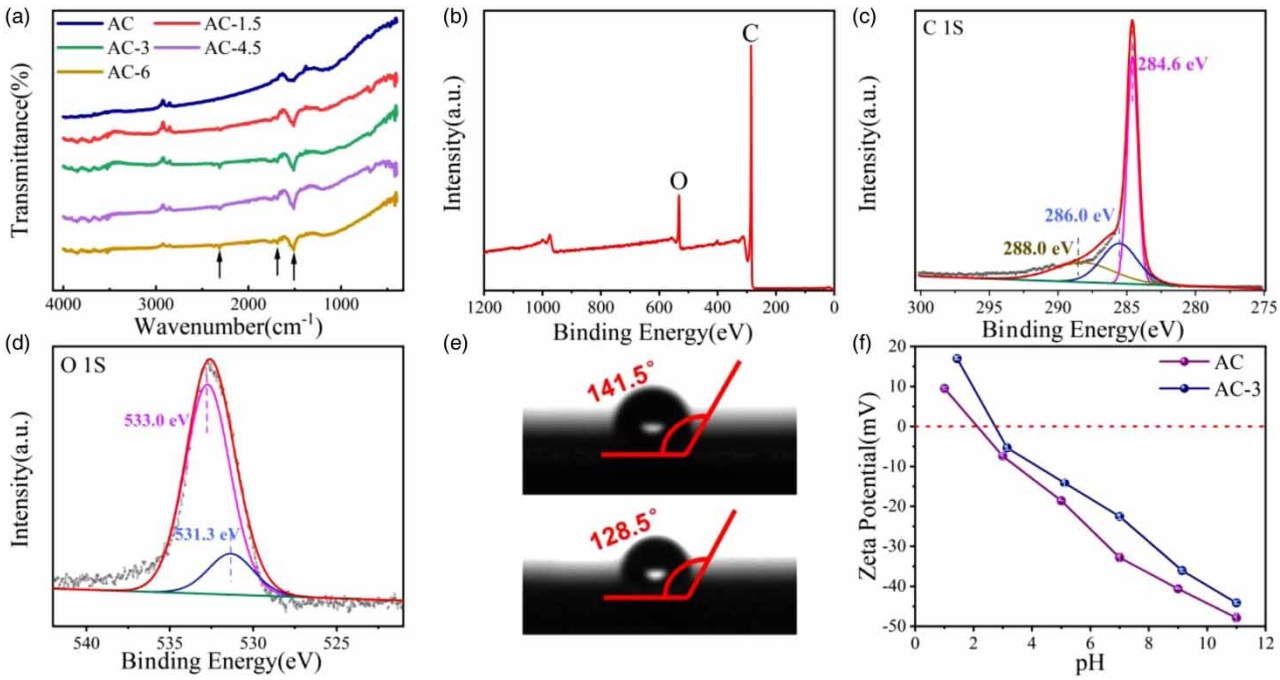

Figure 3 | (a) FTIR spectra of five samples. XPS spectra of AC-x (x = 1.5, 3, 4.5, 6): (b) survey spectrum, (c) C 1 s spectra, (d) O 1 s spectra. (e) Water contact angles of AC and AC-6; (f) zeta potentials of AC and AC-3.

2010). In brief, the carboxyl groups are successfully grafted onto the AC surfaces. The AC surface was greatly modified by increasing the amount of carboxyl groups, which provides more adsorption sites to improve the electrochemical capacitance.

To further verify the surface chemistry and chemical bonding state of the elements, XPS measurements were carried out, as displayed in Figure 3(b)–3(d). The modified materials demonstrate evident C1s and O1s signals (Figure 3(b)). AC-x shows markedly increased carbon–oxygen bonding structures at binding energies ranging from 284 to 290 eV (Huang *et al.* 2014). The deconvolution of the C1s spectra show three peaks at 284.6, 286.0, and 288.0 eV, which correspond to C-C, C-O and C = O, respectively (Figure 3(c)) (Gao *et al.* 2019; Yasin *et al.* 2019; Deka *et al.* 2020). The deconvoluted O1 s spectra, shown in Figure 3(d), can be split into two subpeaks, which represent oxygen atoms double bonded to carbon (C = O at 531.3 eV) and oxygen atoms single bonded to carbon (C-O at 533.0 eV) (Romero-Cano *et al.* 2019; Wang *et al.* 2019). These results reflect the chemical changes on the bare AC surface, which agrees with the FTIR results.

Tests were further carried out by EDS to understand the detailed structure inside the material and the corresponding patterns are shown in Figure S2. The data indicate that the carbon content and the oxygen contents of AC-x both increase, indicating that there are many more carboxylic groups on the surfaces after modification (Gokce & Aktas 2014).

The wettability, an important reference for salt adsorption performance, is reflected by the water contact angle. A material is hydrophilic and hydrophobic when the angle is below and above 90°, respectively. As shown by the photographs of the AC-x surface (Figure 3(e) and Figure S3), the water contact angles of the samples are all above 90°, namely, 138.7° (AC-1.5), 134.0° (AC-3), 132.5° (AC-4.5) and 128.5° (AC-6) affirming the hydrophobicity of the modified materials. Nevertheless, with increasing modification time, the contact angle decreases gradually, with the smallest angle occurring with AC-6. This implies that carboxylic functional groups could improve electrode hydrophilicity, which is beneficial for ion adsorption.

Results of zeta potential measurements for AC and AC-x are shown in Figure 3(f) and Figure S4. The average zeta potential of AC is approximately −30 mV compared with that of the other four modified activated carbons (−16 to −17 mV) when the pH value is 7. This is due to the increase in carboxylic acidic functional group number and the removal of alkaline functional groups in modified materials, which occurs during the destruction of many electrically conducting groups with increasing modification time. These changes are the common outcome of oxidative modification and are reported in former studies (Yao *et al.* 2016; Xu *et al.* 2019). Comparing AC with AC-3 reveals a significant difference in the isoelectric point (IEP) between AC ($pH_{IEP} = 1.9$) and AC-3 ($pH_{IEP} = 2.4$). The high IEP values of AC-3 are ascribed to the existence of carboxyl groups, which further substantiates successful introduction of carboxyl groups (Huang *et al.* 2009; Xu *et al.* 2019).

3.2. Electrochemical characteristics

CV is the main way to evaluate the capacitive characteristics of the prepared electrode. Figure 4(a) and 4(b) and Figure S5 show CV curves of the various materials at varying scanning rates from 5 to 100 mV s^{-1} within the voltage range of −0.4 to 0.8 V. The cyclic voltammograms were similar to rectangles, representing the excellent electrochemical double-layer capacitors of the electrodes (Liu *et al.* 2019; Tan *et al.* 2019). CV splines of the samples still maintain the rectangular shape even at high scan rates of 100 mV s^{-1}, indicating their high rate capability. Figure 4(c) shows the CV splines of the materials at a scan rate of 10 mV s^{-1}. As the specific capacitance is proportional to the CV curve area, the specific capacitance values of the electrodes at various scan rates are calculated by integrating the voltammetric charge in the CV curves (Kyaw *et al.* 2020). AC-1.5 has the largest specific capacitance of about 67.14 F g^{-1}, and AC-6 has the lowest specific capacitance at around 14.51 F g^{-1}. The high specific capacitance of AC-1.5 is attributed to its high specific surface area and large percentages of mesopores. Specifically, the specific capacitances of AC-x tend to decrease with increasing modification time.

Figure 4(d) exhibits the specific capacitances of AC and AC-x deducted from CV at different scan rates. The specific capacitances of the samples gradually decrease with increasing scan rate, which is attributed to the decreasing degree order of the double layers as the diffusion rate of ions increases (Adorna *et al.* 2020; Sufiani *et al.* 2020). The corresponding specific capacitances reveal that AC-x (x = 1.5, 3, 4.5) have better capacitances than AC. AC-1.5 delivers a substantially higher specific capacitance not only at 5 mV s^{-1} but also at 100 mV s^{-1}, implicating its increased ionic diffusion and adsorption. Meanwhile, AC-1.5 has the highest capacitance retention of around 34.75%, revealing a higher specific capacity and better ratio characteristics. In a sense, AC-1.5 has appropriate pore structure. Therefore, it displays higher capacitance. AC-6 shows the lowest capacitance because of the collapse of the pore structure. Generally, after treatment, as the pore size distribution is optimized, this change can ultimately lead to increased capacitance. Table 2 shows that the proposed anode electrode exhibits a higher specific capacitance than other electrodes previously reported in the literature.

The GCD curves of electrodes at different current densities (0.5–10 A g^{-1}) are exhibited in Figure 5(a) and 5(b) and Figure S5. The results reveal that the GCD curves of all samples at all current densities exhibit the typical symmetrical triangular shape, representing the EDLCs mechanism. Thus, all samples have good charge-discharge properties. As the current density increases, the charge and discharge times subsequently decrease, revealing that the electrodes follow representative

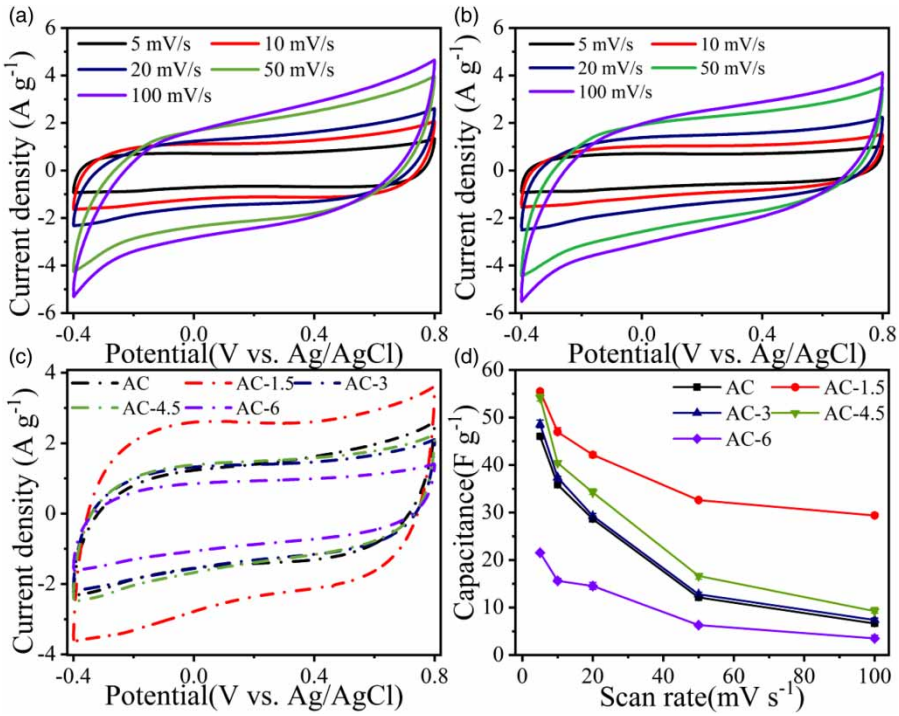

Figure 4 | CV of the various samples at different scan rates. (a) AC, (b) AC-3, (c) CV curves of five electrodes at 10 mV s^{-1}, and (d) specific capacity results from CV at different scan rates.

Table 2 | Comparison of the specific capacitance of different materials

Material	Voltage (V)	Specific capacitance (F g^{-1})	Refs
Porous carbon	1.0	56.01	Liu *et al.* (2019)
Activated carbon	1.0	49.82	Haq *et al.* (2020)
One-dimensional V_2O_5	1.2	59.50	Liu *et al.* (2021a)
Graphene hollow shells	1.2	39.28	Zhu *et al.* (2020)
$Na_3V_2(PO_4)_3$@C	1.0	41.27	Cao *et al.* (2019)
Activated carbon	1.2	67.14	This work

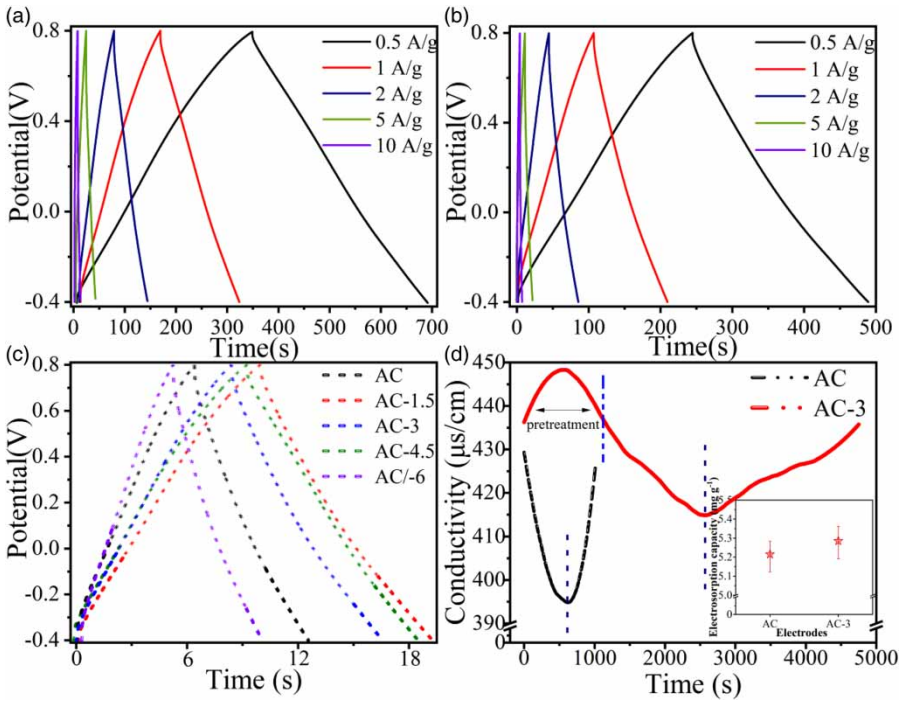

Figure 5 | GCD curves of (a) AC and (b) AC-3, (c) GCD curves of the five electrodes at a current density of 10 A g^{-1}, and (d) variation in the solution conductivity vs. time of AC and AC-3 (the inset illustrates the desalination capacity of the two samples).

capacitive behavior for electroadsorbed ions (Deka *et al.* 2020; Liu *et al.* 2021b). Figure 5(c) shows the GCD curves of the electrodes at a current density of 10 A g^{-1}. All the samples display a triangular shape, indicating acceptable double-layer capacitance performance and excellent reversibility during the constant current density charge-discharge test. Compared to the other materials, AC-1.5 has the longest discharge time, showing the best capacitive performance. In contrast, AC-6 has the lowest specific capacitance. These results are consistent with the CV results.

3.3. Desalination performance of the capacitive deionization cell

The desalination performances of AC and AC-x over time were tested in a NaCl solution. The changes in the conductivity and current of the solution are presented in Figure 5(d), Figures S5 and S6, respectively. The current passing through AC-x (x = 1.5, 3, 4.5) is higher than that passing through AC, indicating that the ion migration rate increases after modification. This is associated with the rich aperture structure and excellent electrical conductivity of AC-x, demonstrating their good double-layer capacitance and high SAC (Mao *et al.* 2021).

Regarding AC, the conductivity of the solution goes down rapidly at first, indicating the rapid adsorption of Na^+ and Cl^- ions by a large number of available adsorption sites. Over time, the conductivity decreases moderately as most of the ions are

adsorbed, and then the conductivity decreases to a minimum. Electrodes are the short-circuited and the original electric field disappears. Due to the formation of opposite electrical properties of EDLCs and existence of inside potential difference between the anodes and cathodes, the electrodes are in a state of discharging. This causes the ions to move from electrodes back to the solution, thereby realizing charge neutralization and decreasing the potential difference between the two poles. Ions are gradually released back into the solution, so the conductivity of the solution and the concentration of ions in the solution gradually increases. The conductivity returns to its original state when all the adsorbed ions are released, finally achieving charge neutralization (Yeh *et al.* 2015; Gao *et al.* 2019).

Regarding AC-x, the conductivity curves show similar characteristics, and the electrodes also effectively adsorb the anions in the solution. Nevertheless, as the carboxyl groups and anions are negatively charged, the carboxyl groups are likely to initially repel some anions that are distributed at sites of high carboxyl group content or near the carboxyl groups. Meanwhile, anions may suffer stronger electrostatic repulsion at these sites, resulting in ion release. Thus, pretreatment is conducted during the experiment to avoid ion release and conductivity fluctuations during the initial stage. During the pretreatment process, those repelled anions may re-enter the sites with lower electrostatic repulsion, thereby realizing redistribution of ion adsorption and desorption sites in the materials. Afterwards, the ions that achieved site redistribution and the rest of the ions originally existed could subsequently complete the adsorption/desorption process. AC-3 takes only around 1,600 s to reach equilibrium, indicating that it had a better desalination performance than the others. This is corroborated by the higher electrosorption capacity of AC-3 than that of AC (inset of Figure 5(d)) (Han *et al.* 2020). Evidently, although the co-ion expulsion effect is probably enhanced when AC-x is used as the anode in CDI, anions could still be effectively adsorbed onto the electrode.

3.4. Selective electroadsorption of phosphate by AC-x electrodes

Selective electroadsorption experiments were conducted in an anion coexistence system. Figure 6(a)–6(e) exhibit the individual and total anion adsorption capacity changes of Cl^-, PO_4^{3-}, and SO_4^{2-} on AC and AC-x with respect to time. The dissolution of Cl^- is increasingly obvious in the initial stage as the modification time increases while this phenomenon is not observed with PO_4^{3-}, proving that the carboxyl groups have an affinity for PO_4^{3-}. SO_4^{2-} could not be adsorbed by the modified materials, which benefits PO_4^{3-} adsorption because PO_4^{3-} and SO_4^{2-} have similar adsorption sites (Wu *et al.* 2020). According to the

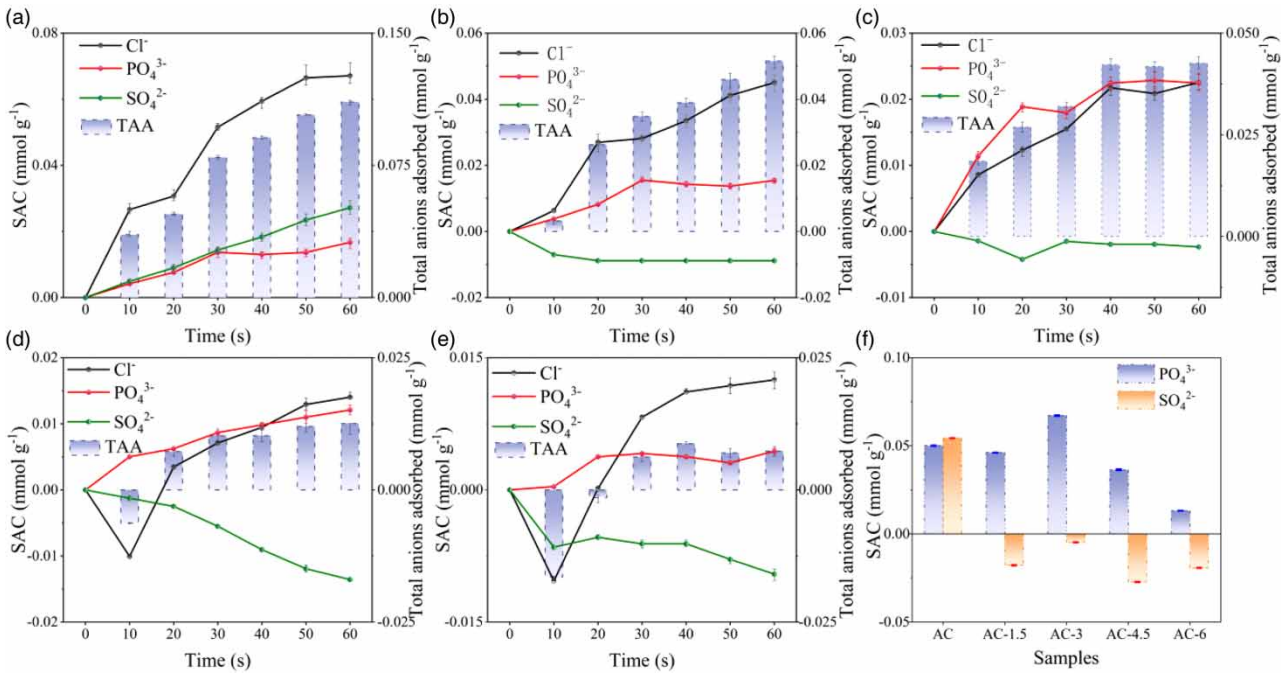

Figure 6 | Individual anion adsorption capacity of Cl^-, PO_4^{3-} and SO_4^{2-} and the total adsorption capacity of three anions (TAA) over time: (a) AC, (b) AC-1.5, (c) AC-3, (d) AC-4.5, and (e) AC-6. (f) Normalized equivalent capacity of PO_4^{3-} and SO_4^{2-}.

normalized equivalent capacity (valence * adsorption amount) (Hou & Huang 2013), the competitive adsorption capacity of SO_4^{2-} is far below that of PO_4^{3-} (Figure 6(f)). Thus, competitive electric adsorption occurs between SO_4^{2-} and PO_4^{3-}.

The sum of the ion adsorption capacity decreases gradually with increasing modification time (Figure S7). The total amount of anions adsorbed in the five reactors reaches average values of about 0.26, 0.15, 0.10, 0.07, and 0.02 mmol g^{-1}, with phosphate accounting for 15.07%, 29.87%, 52.65%, 46.32%, and 26.07%, respectively. The pore structure of the materials clearly becomes more glazed after modification, which decreases the internal diffusion resistance. Therefore, anions are more violently repelled by carboxyl groups as both are negatively charged when the anions entered the adsorption sites, leading to an increase in ionic diffusion and a decrease in the ion adsorption capacity. For further study, the selectivity of the five electrodes toward PO_4^{3-} was demonstrated (Figure 7(a)). The changes in the trend of phosphate selectivity of each modified material is particularly consistent with that of the carboxyl content observed by Boehm titration (Figure 7(b)) (Huang *et al.* 2009). The higher is the carboxyl group content, the higher is the selective coefficient. AC-3 has the highest phosphate selectivity corresponding to the highest carboxyl group content.

Considering the phenomena observed, the selective adsorption mechanism can be explained. For AC, chloride ions and sulphate have a higher electrosorption capacity than phosphate. This may be because the electronegativity of phosphorus (2.19) is lower than that of sulphur (2.58) and chlorine (3.16), which is consistent with the results in previous studies (Tang *et al.* 2017; Jiang *et al.* 2019). As for AC-x, when the operational conditions are the same, the selectivity is based on the ion properties, namely, its hydrated size and valence (Mossad *et al.* 2013; Chen *et al.* 2015). Obvious competitive adsorption occurs between sulphate and phosphate in the work because both of them have similar adsorption sites. Ions with a smaller hydration radius are more likely to enter the surface pores to complete adsorption as the pore resistance is smaller under this circumstance (Wu *et al.* 2020). It has been experimentally proven that the hydration radii of the ions are as follows: PO_4^{3-} (0.339 nm) (Tansel 2012) < SO_4^{2-} (0.379 nm) (Li *et al.* 2016), leading to the preferential adsorption of PO_4^{3-}. Meanwhile, for ions with different valences, the material preferentially adsorbs the ion with the highest valence (Seo *et al.* 2010). Thus, phosphate may be preferentially adsorbed in an electric field. Moreover, compared with other two ions, the bond polarity of PO_4^{3-} is stronger. PO_4^{3-}, as a hydrogen donor, can form a stronger hydrogen bond with the carboxyl group that acts as a hydrogen acceptor, achieving highly selective adsorption and separating it from other anions that do not contain hydrogen (Wu *et al.* 2020). Additionally, the charge advantage of sulphate is partially offset by the increase in carboxyl groups after modification, resulting in a lower sulphate adsorption capacity. As shown in Figure 8, on the basis of prior studies,

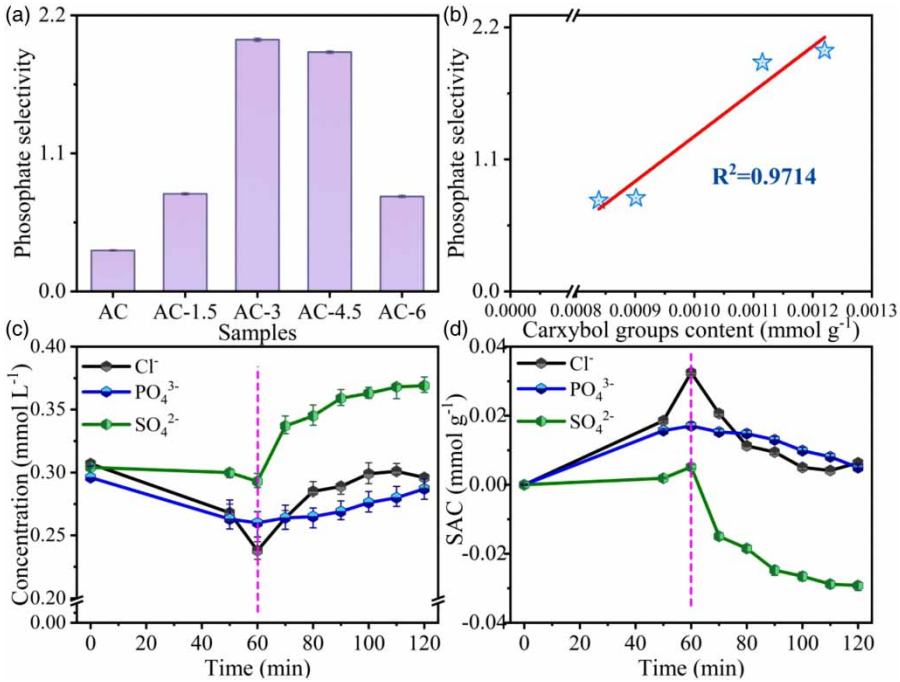

Figure 7 | (a) Phosphate selectivity of the five electrodes, (b) correlation analysis of the carboxyl group content and phosphate selectivity coefficient, (c) concentration and (d) mass removal of three anions during the electrosorption/desorption process.

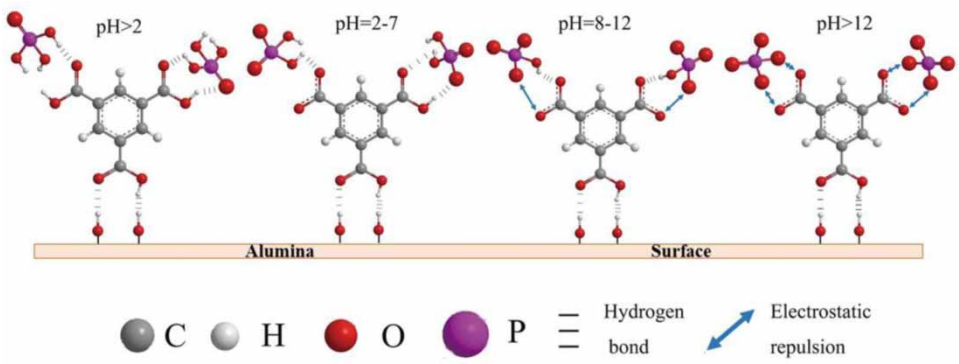

Figure 8 | Mechanism of selective adsorption of phosphate.

it is important to mention that when the pH of the solution is below 2, both carboxyl groups and PO_4^{3-} have no electrical charge. Therefore, the selective adsorption of PO_4^{3-} on carboxyl-modified electrodes relies on weak hydrogen bonds during the protonation process (Wu *et al.* 2020; Li *et al.* 2021). As the pH increases, the protonation of the carboxyl groups and PO_4^{3-} gradually decreases, resulting in stronger hydrogen bonding and electrostatic repulsion between the two (Zhu *et al.* 2019; Wu *et al.* 2020). Overall, the adsorption process principally depends on weak hydrogen bonds when two types of forces coexist. In short, carboxyl-modified materials can attain the goal of a consistent adsorption effect within a wide pH range attributed to hydrogen bond interactions.

3.5. Desorption

As AC-3 exhibits the peak phosphate selectivity, after 60 min of adsorption in this reactor, this reactor was switched to short circuit for 1 h of desorption with the solution containing Cl^-, PO_4^{3-}, and SO_4^{2-} at a concentration of 0.8 mmol·L^{-1}. The content and mass removal of TAA during the electrosorption/desorption process are illustrated in Figure 7(c) and 7(d). With increasing operation time during the 120-min adsorption/desorption process, Cl^- and PO_4^{3-} are notably desorbed in the desorption process with an applied short circuit. In contrast, SO_4^{2-} is not adsorbed well and the sulphate ions originally contained in AC are constantly released in the desorption process due to repelling. Therefore, SO_4^{2-} concentration in the solution gradually increases and the desorption efficiency of SO_4^{2-} cannot be accurately calculated. The desorption efficiency of PO_4^{3-} is 72.12% after 2 h of electrosorption/desorption, indicating that AC-3 has a strong and effective selective adsorption ability for removing phosphate from water. This experiment reveals the distinct selectivity and suitable regeneration of AC-3 in the desorption procedure, which is a key factor for its practical applications in wastewater treatment.

3.6. Stability

Cycling stability is a crucial factor determining whether the electrode can be applied in practice. The long-term cycling stability of AC-3 was estimated in a three-electrode system. As depicted in Figure 9(a), the cyclic voltammograms remain rectangular in shape throughout 1,000 cycles, illustrating its good cycling stability (Tian *et al.* 2021). The corresponding specific capacitance shows a gradual increase with an increasing cycle number, eventually reaching 551% of the initial specific capacitance at the 1,000th cycle (Figure 9(b)), which suggests that AC-3 has excellent electrochemical performance. This result might be attributed to the existence of more electrochemical active sites that originate from the decrease in end groups in AC-3 after nitric acid oxidation.

The electrochemical stability and CDI cycling performance of AC-3 were tested for 1,000 GCD cycles at a current density of 10 mA g^{-1}, and the results are illustrated in Figure 9(c). The first three cycles, the middle three cycles and the last three cycles still maintain a traditional symmetrical triangular shape during the process. Additionally, almost complete retention of the specific capacitance is observed in the repeated cycle, which further demonstrates that the electrode shows fantastic cycling performance over charge-discharge cycling of the device (Wang *et al.* 2019). AC-3 has excellent cyclability and remarkable stability, which is a valuable reference for evaluating its long-term successful application in CDI.

Compared with the other materials, AC-3 exhibits superior CDI performance. Therefore, we calculated the cycling desalination stability and regeneration capacities of AC-3 with an original saline water concentration of 1,000 mg L^{-1} over 5 cycles. As mentioned previously, pretreatment is required in the initial phase. The conductivity exhibits similar changes of first

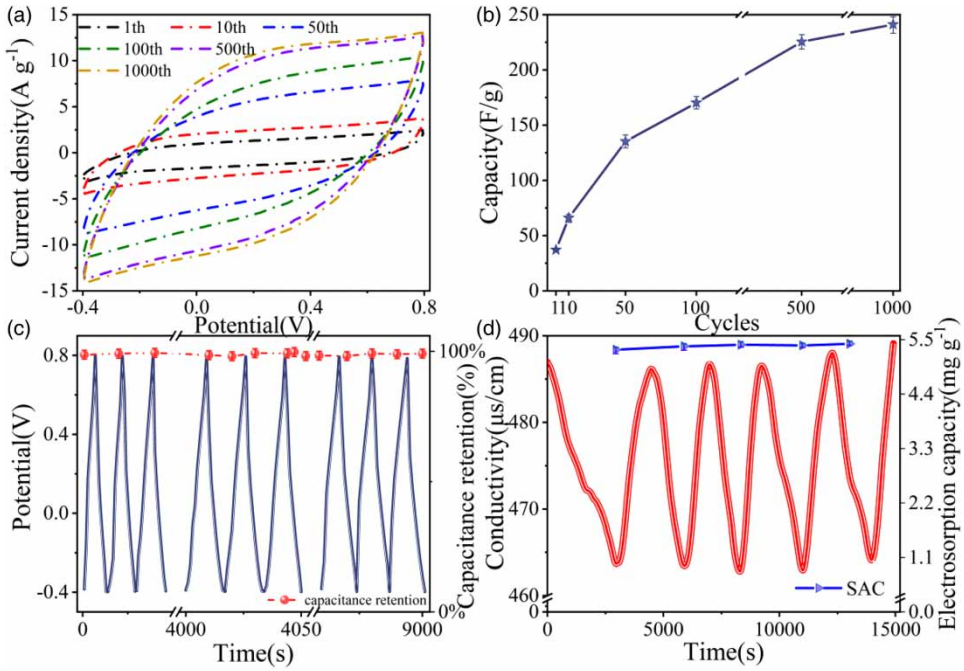

Figure 9 | (a) CV cycling performance of AC-3 at a scan rate of 10 mV s^{-1}, (b) specific capacitance of AC-3 in the cycling test at a scan rate of 10 mV s^{-1}, (c) galvanostatic cycling stability of the facility at a current density of 10 mA g^{-1} with the first, middle and last 3 CGD cycles inserted, and (d) CDI profile of the electrosorption/desorption cycles and cycling stability of AC-3 in 1 mM NaCl solution.

descending because the electrolytes are attracted to the electrodes with opposite charges and then ascending due to the desorption of the adsorbed salt ions (Gao *et al.* 2019; Zhang *et al.* 2020). No significant decline in desalination performance was observed after five continuous cycles, and the retained SAC resembles the capacitance retention rate (Figure 9(d)). This indicates that AC-3 has splendid long-term cycling stability and outstanding regeneration performance after electrosorption/desorption cycles.

4. CONCLUSIONS

To summarize, carboxyl-modified AC with various treatment times was resoundingly developed for selective phosphate removal from ternary anion mixed solutions. AC-3 exhibited high surface area of 681 $m^2 g^{-1}$, reasonable electrochemical property of specific capacitance at 49.08 F g^{-1}, proper SAC of 5.35 mg g^{-1}, especially excellent selectivity for phosphate of 2.01 which was six times higher than that of AC in the presence of coexisting ions of chloride ions, phosphate ions and sulphate ions. Desorption results of AC-3 electrode also showed that 72.12% of phosphate could be desorbed under short-circuited-mode condition. Additionally, AC-3 also exhibited outstanding long-term stability and excellent regeneration performance during cycling experiments. Taken together, these properties underpin the potential applicability of using AC-3 as an electrode material to improve phosphate selective adsorption performance from mixed anions water. Mechanistically, apart from the ionic valence state, ionic hydration radius, and electronegativity, phosphate selective adsorption could be mainly attributed to hydrogen-bond interactions. Specifically, phosphate, as a hydrogen donor, could form a stronger hydrogen bond with the carboxyl group that acted as a hydrogen acceptor in AC-3, and the high adsorption selectivity in AC-3 is in line with its high carboxyl group content. The selectivity of these asymmetric electrodes is not limited to phosphate, and similar methods for other anions may be possible. This study provides a fundamental basis for the selective adsorption of anions in real water treatment applications.

AUTHOR CONTRIBUTION

Luwei Miao: Conceptualization, Methodology, Software, Investigation, Writing – original draft. **Wenyang Deng**: Validation, Formal analysis, Visualization. **Xiaohong Chen**: Validation, Formal analysis, Visualization. **Ming Gao**: Formal analysis, Visualization. **Wenqing Chen**: Resources, Writing – review and editing, Supervision. **Tianqi Ao**: Writing–review and editing.

DECLARATION OF COMPETING INTEREST

The authors declare that they have no known competing financial interests or personal relationships that could have appeared to influence the work reported in this paper.

ACKNOWLEDGEMENTS

This research did not receive any specific grant from funding agencies in the public, commercial, or not-for-profit sectors. We appreciate Wang Hui from the Analytical & Testing Center of Sichuan University for assistance with SEM characterization.

DATA AVAILABILITY STATEMENT

Data cannot be made publicly available; readers should contact the corresponding author for details.

REFERENCES

Adorna, J., Borines, M., Dang, V. D. & Doong, R.-A. 2020 Coconut shell derived activated biochar–manganese dioxide nanocomposites for high performance capacitive deionization. *Desalination* **492**, 114602. https://doi.org/10.1016/j.desal.2020.114602.

Cao, J., Wang, Y., Wang, L., Yu, F. & Ma, J. 2019 $Na_3V_2(PO_4)_3$@C as faradaic electrodes in capacitive deionization for high-performance desalination. *Nano Letters* **19** (2), 823–828.

Chen, J. P., Wu, S. & Chong, K.-H. 2003 Surface modification of a granular activated carbon by citric acid for enhancement of copper adsorption. *Carbon* **41** (10), 1979–1986.

Chen, Z., Zhang, H., Wu, C., Wang, Y. & Li, W. 2015 A study of electrosorption selectivity of anions by activated carbon electrodes in capacitive deionization. *Desalination* **369**, 46–50.

Deka, N., Barman, J., Kasthuri, S., Nutalapati, V. & Dutta, G. K. 2020 Transforming waste polystyrene foam into N-doped porous carbon for capacitive energy storage and deionization applications. *Applied Surface Science* **511**, 145576. https://doi.org/10.1016/j.apsusc.2020.145576.

Gao, T., Du, Y. & Li, H. 2019 Preparation of nitrogen-doped graphitic porous carbon towards capacitive deionization with high adsorption capacity and rate capability. *Separation and Purification Technology* **211**, 233–241.

Gokce, Y. & Aktas, Z. 2014 Nitric acid modification of activated carbon produced from waste tea and adsorption of methylene blue and phenol. *Applied Surface Science* **313**, 352–359.

Han, D.-C., Zhang, C.-M., Guan, J., Gai, L.-H., Yue, R.-Y., Liu, L.-N., Afzal, M. Z., Song, C., Wang, S.-G. & Sun, X.-F. 2020 High-performance capacitive deionization using nitrogen and phosphorus-doped three-dimensional graphene with tunable pore size. *Electrochimica Acta* **336**, 135639. https://doi.org/10.1016/j.electacta.2020.135639.

Haq, O. U., Choi, D.-S., Choi, J.-H. & Lee, Y.-S. 2020 Carbon electrodes with ionic functional groups for enhanced capacitive deionization performance. *Journal of Industrial and Engineering Chemistry* **83**, 136–144.

He, J., Yang, Y., Xu, Y., Wang, Z., Xu, B., Huang, Y. & Yang, L. 2020 $La(OH)_3$ nano-rods/polyacrylonitrile nanofibers: fabrication, characterization and application for phosphate removal. *Water Science and Technology* **82** (10), 2098–2113.

Hong, S. P., Yoon, H., Lee, J., Kim, C., Kim, S., Lee, J., Lee, C. & Yoon, J. 2020 Selective phosphate removal using layered double hydroxide/reduced graphene oxide (LDH/rGO) composite electrode in capacitive deionization. *Journal of Colloid and Interface Science* **564**, 1–7.

Hou, C.-H. & Huang, C.-Y. 2013 A comparative study of electrosorption selectivity of ions by activated carbon electrodes in capacitive deionization. *Desalination* **314**, 124–129.

Huang, G., Shi, J. X. & Langrish, T. A. G. 2009 Removal of Cr(VI) from aqueous solution using activated carbon modified with nitric acid. *Chemical Engineering Journal* **152** (2–3), 434–439.

Huang, W., Zhang, Y., Bao, S., Cruz, R. & Song, S. 2014 Desalination by capacitive deionization process using nitric acid-modified activated carbon as the electrodes. *Desalination* **340**, 67–72.

Jiang, J., Kim, D. I., Dorji, P., Phuntsho, S., Hong, S. & Shon, H. K. 2019 Phosphorus removal mechanisms from domestic wastewater by membrane capacitive deionization and system optimization for enhanced phosphate removal. *Process Safety and Environmental Protection* **126**, 44–52.

Kim, Y. J. & Choi, J. H. 2012 Selective removal of nitrate ion using a novel composite carbon electrode in capacitive deionization. *Water Research* **46** (18), 6033–6039.

Kyaw, H. H., Myint, M. T. Z., Al-Harthi, S. & Al-Abri, M. 2020 Removal of heavy metal ions by capacitive deionization: effect of surface modification on ions adsorption. *Journal of Hazardous Materials* **385**, 121565.

Lei, Y., Zhan, Z., Saakes, M., van der Weijden, R. D. & Buisman, C. J. N. 2021 Electrochemical recovery of phosphorus from acidic cheese wastewater: feasibility. *Quality of Products, and Comparison with Chemical Precipitation. ACS ES&T Water* **1** (4), 1002–1013.

Li, H., Liang, S., Gao, M., Li, G., Li, J. & He, L. 2014 The study of capacitive deionization behavior of a carbon nanotube electrode from the perspective of charge efficiency. *Water Science and Technology* **71** (1), 83–88.

Li, Y., Zhang, C., Jiang, Y., Wang, T.-J. & Wang, H. 2016 Effects of the hydration ratio on the electrosorption selectivity of ions during capacitive deionization. *Desalination* **399**, 171–177.

Li, J., Fang, X., Yang, M., Tan, W., Zhang, H., Zhang, Y., Li, G. & Wang, H. 2021 The adsorption properties of functionalization vetiver grass-based activated carbon: the simultaneous adsorption of phosphate and nitrate. *Environmental Science and Pollution Research International* **28**, 40544–40554. https://doi.org/10.1007/s11356-020-09271-5.

Liu, X., Zong, E., Hu, W., Song, P., Wang, J., Liu, Q., Ma, Z. & Fu, S. 2018 Lignin-derived porous carbon loaded with $La(OH)_3$ nanorods for highly efficient removal of phosphate. *ACS Sustainable Chemistry & Engineering* **7** (1), 758–768.

Liu, Q., Li, X., Wu, Y., Qing, M., Tan, G. & Xiao, D. 2019 Pine pollen derived porous carbon with efficient capacitive deionization performance. *Electrochimica Acta* **298**, 360–371.

Liu, X., Shanbhag, S., Bartholomew, T. V., Whitacre, J. F. & Mauter, M. S. 2020 Cost comparison of capacitive deionization and reverse osmosis for brackish water desalination. *ACS ES&T Engineering* **1** (2), 261–273.

Liu, B., Yu, L., Yu, F. & Ma, J. 2021a In-situ formation of uniform V_2O_5 nanocuboid from V_2C MXene as electrodes for capacitive deionization with higher structural stability and ion diffusion ability. *Desalination* **500**, 114897. https://doi.org/10.1016/j.desal.2020.114897.

Liu, L., Zhao, C., Zheng, F., Deng, D., Anderson, M. A. & Wang, Y. 2021b Three-dimensional electrode design with conductive fibers and ordered macropores for enhanced capacitive deionization performance. *Desalination* **498**, 114794. https://doi.org/10.1016/j.desal.2020.114794.

Mao, M., Yan, T., Chen, G., Zhang, J., Shi, L. & Zhang, D. 2021 Selective capacitive removal of Pb^{2+} from wastewater over redox-active electrodes. *Environmental Science & Technology* **55** (1), 730–737.

Mohamed, S. K., Abuelhamd, M., Allam, N. K., Shahat, A., Ramadan, M. & Hassan, H. M. A. 2020 Eco-friendly facile synthesis of glucose–derived microporous carbon spheres electrodes with enhanced performance for water capacitive deionization. *Desalination* **477**, 114278. https://doi.org/10.1016/j.desal.2019.114278.

Mossad, M., Zhang, W. & Zou, L. 2013 Using capacitive deionisation for inland brackish groundwater desalination in a remote location. *Desalination* **308**, 154–160.

Paltrinieri, L., Huerta, E., Puts, T., van Baak, W., Verver, A. B., Sudhölter, E. J. R. & de Smet, L. C. P. M. 2019 Functionalized anion-exchange membranes facilitate electrodialysis of citrate and phosphate from model dairy wastewater. *Environmental Science & Technology* **53** (5), 2396–2404.

Roh, J. S., Park, J.-S., Roh, J. M., Park, H. B. & Do, S.-H. 2018 The pretreatment of granular activated carbon using sodium persulfate and hydrogen peroxide under basic conditions: properties, metal impregnation, and As(V) adsorption. *Materials Chemistry and Physics* **218**, 317–325.

Romero-Cano, L. A., Zárate-Guzmán, A. I., Carrasco-Marín, F. & González-Gutiérrez, L. V. 2019 Electrochemical detection of copper in water using carbon paste electrodes prepared from bio-template (grapefruit peels) functionalized with carboxyl groups. *Journal of Electroanalytical Chemistry* **837**, 22–29.

Sakamoto, T., Amano, Y. & Machida, M. 2020 Phosphate ion adsorption properties of PAN-based activated carbon fibers prepared with K_2CO_3 activation. *SN Applied Sciences* **2** (4), 702. https://doi.org/10.1007/s42452-020-2465-1.

Seo, S.-J., Jeon, H., Lee, J. K., Kim, G.-Y., Park, D., Nojima, H., Lee, J. & Moon, S.-H. 2010 Investigation on removal of hardness ions by capacitive deionization (CDI) for water softening applications. *Water Research* **44** (7), 2267–2275.

ShamsiJazeyi, H. & Kaghazchi, T. 2010 Investigation of nitric acid treatment of activated carbon for enhanced aqueous mercury removal. *Journal of Industrial and Engineering Chemistry* **16** (5), 852–858.

Shi, J., Li, W. & Li, D. 2015 Rapidly reversible adsorption of methane with a high storage capacity on the zeolite templated carbons with glucose as carbon precursors. *Colloids and Surfaces A: Physicochemical and Engineering Aspects* **485**, 11–17.

Song, Y., Yuan, P., Wei, Y., Liu, D., Tian, Q., Zhou, J., Du, P., Deng, L., Chen, F. & Wu, H. 2019 Constructing hierarchically porous nestlike Al_2O_3–MnO_2@Diatomite composite with high specific surface area for efficient phosphate removal. *Industrial & Engineering Chemistry Research* **58** (51), 23166–23174.

Sufiani, O., Tanaka, H., Teshima, K., Machunda, R. L. & Jande, Y. A. C. 2020 Enhanced electrosorption capacity of activated carbon electrodes for deionized water production through capacitive deionization. *Separation and Purification Technology* **247**, 116998. https://doi.org/10.1016/j.seppur.2020.116998.

Sun, J., Mu, Q., Wang, T., Qi, J. & Hu, C. 2021 Selective electrosorption of Ca^{2+} by MXene cathodes coupled with NiAl-LMO anodes through ion intercalation. *Journal of Colloid and Interface Science* **590**, 539–547.

Tan, G., Liu, Q., Li, X., Liu, Y. & Xiao, D. 2019 Porous carbon material prepared from Na_2EDTA and its performance in capacitive deionization process. *Applied Surface Science* **496**, 143526. https://doi.org/10.1016/j.apsusc.2019.07.268.

Tang, W., He, D., Zhang, C. & Waite, T. D. 2017 Optimization of sulfate removal from brackish water by membrane capacitive deionization (MCDI). *Water Research* **121**, 302–310.

Tansel, B. 2012 Significance of thermodynamic and physical characteristics on permeation of ions during membrane separation: hydrated radius, hydration free energy and viscous effects. *Separation and Purification Technology* **86**, 119–126.

Tian, S., Zhang, X. & Zhang, Z. 2021 Novel MoS_2/NOMC electrodes with enhanced capacitive deionization performances. *Chemical Engineering Journal* **409**, 128200. https://doi.org/10.1016/j.cej.2020.128200.

Verlicchi, P. & Zambello, E. 2015 Pharmaceuticals and personal care products in untreated and treated sewage sludge: occurrence and environmental risk in the case of application on soil – A critical review. *Science of The Total Environment* **538**, 750–767.

Wang, C., Chen, L., Liu, S. & Zhu, L. 2018 Nitrite desorption from activated carbon fiber during capacitive deionization (CDI) and membrane capacitive deionization (MCDI). *Colloids and Surfaces A: Physicochemical and Engineering Aspects* **559**, 392–400.

Wang, A., Sun, K., Li, J., Xu, W. & Jiang, J. 2019 Nitrogen and oxygen dual-doped activated carbon as electrode material for high performance supercapacitors prepared by direct carbonization of amaranthus. *Materials Chemistry and Physics* **231**, 311–321.

Wu, B., Wan, J., Zhang, Y., Pan, B. & Lo, I. M. C. 2020 Selective phosphate removal from water and wastewater using sorption: process fundamentals and removal mechanisms. *Environmental Science & Technology* **54** (1), 50–66.

Wu, S., Yan, P., Yang, W., Zhou, J., Wang, H., Che, L. & Zhu, P. 2021 $ZnCl_2$ enabled synthesis of activated carbons from ion-exchange resin for efficient removal of Cu^{2+} ions from water via capacitive deionization. *Chemosphere* **264** (Pt 2), 128557. https://doi.org/10.1016/j.chemosphere.2020.128557.

Xiao, N., Tan, H., Zhu, J., Tan, L., Rui, X., Dong, X. & Yan, Q. 2013 High-performance supercapacitor electrodes based on graphene achieved by thermal treatment with the aid of nitric acid. *ACS Applied Materials & Interfaces* **5** (19), 9656–9662.

Xing, W., Liang, J., Tang, W., He, D., Yan, M., Wang, X., Luo, Y., Tang, N. & Huang, M. 2020 Versatile applications of capacitive deionization (CDI)-based technologies. *Desalination* **482**, 114390.

Xu, H., Yuan, H., Yu, J. & Lin, S. 2019 Study on the competitive adsorption and correlational mechanism for heavy metal ions using the carboxylated magnetic iron oxide nanoparticles (MNPs-COOH) as efficient adsorbents. *Applied Surface Science* **473**, 960–966.

Yao, S., Zhang, J., Shen, D., Xiao, R., Gu, S., Zhao, M. & Liang, J. 2016 Removal of Pb(II) from water by the activated carbon modified by nitric acid under microwave heating. *Journal of Colloid and Interface Science* **463**, 118–127.

Yasin, A. S., Jeong, J., Mohamed, I. M. A., Park, C. H. & Kim, C. S. 2017 Fabrication of N-doped &SnO_2-incorporated activated carbon to enhance desalination and bio-decontamination performance for capacitive deionization. *Journal of Alloys and Compounds* **729**, 764–775.

Yasin, A. S., Mohamed, I. M. A., Amen, M. T., Barakat, N. A. M., Park, C. H. & Kim, C. S. 2019 Incorporating zirconia nanoparticles into activated carbon as electrode material for capacitive deionization. *Journal of Alloys and Compounds* **772**, 1079–1087.

Yeh, C.-L., Hsi, H.-C., Li, K.-C. & Hou, C.-H. 2015 Improved performance in capacitive deionization of activated carbon electrodes with a tunable mesopore and micropore ratio. *Desalination* **367**, 60–68.

Yu, C., Fan, X., Yu, L., Bandosz, T. J., Zhao, Z. & Qiu, J. 2013 Adsorptive removal of thiophenic compounds from oils by activated carbon modified with concentrated nitric acid. *Energy & Fuels* **27** (3), 1499–1505.

Zhang, R., Gu, X., Liu, Y., Hua, D., Shao, M., Gu, Z., Wu, J., Zheng, B., Zhang, W., Li, S., Huo, F. & Huang, W. 2020 Hydrophilic nanoporous carbon derived from egg whites for highly efficient capacitive deionization. *Applied Surface Science* **512**. https://doi.org/10.1016/j.apsusc.2020.145740.

Zhang, C., Wang, M., Xiao, W., Ma, J., Sun, J., Mo, H. & Waite, T. D. 2021 Phosphate selective recovery by magnetic iron oxide impregnated carbon flow-electrode capacitive deionization (FCDI). *Water Research* **189**, 116653. https://doi.org/10.1016/j.watres.2020.116653.

Zhao, C., Zhang, L., Ge, R., Zhang, A., Zhang, C. & Chen, X. 2019 Treatment of low-level Cu(II) wastewater and regeneration through a novel capacitive deionization-electrodeionization (CDI-EDI) technology. *Chemosphere* **217**, 763–772.

Zhao, X., Wei, H., Zhao, H., Wang, Y. & Tang, N. 2020 Electrode materials for capacitive deionization: a review. *Journal of Electroanalytical Chemistry* **873**, 114416. http://dx.doi.org/10.1016/j.jelechem.2020.114416.

Zheng, D., Yao, R., Sun, C., Zheng, Y. & Liu, C. 2021 Highly efficient low-concentration phosphate removal from effluents by recoverable $La(OH)_3$/Foamed nickel adsorbent. *ACS Omega* **6** (8), 5399–5407.

Zhu, E., Hong, X., Ye, Z., Hui, K. S. & Hui, K. N. 2019 Influence of various experimental parameters on the capacitive removal of phosphate from aqueous solutions using LDHs/AC composite electrodes. *Separation and Purification Technology* **215**, 454–462.

Zhu, Y., Zhang, G., Xu, C. & Wang, L. 2020 Interconnected graphene hollow shells for high-performance capacitive deionization. *ACS Applied Materials & Interfaces* **12** (26), 29706–29716.

First received 15 July 2021; accepted in revised form 24 August 2021. Available online 6 September 2021